Submesoscale processes in the Kuroshio Loop Current: roles in energy cascade and salt and heat transports

Tian Tang[1,2,3], Zhiwei Zhang[1,2*], Jinchao Zhang[1,2], Xincheng Zhang[1,2], Zhongbin Sun[1,2], and Zhe Feng[1,2]

[1]Frontier Science Center for Deep Ocean Multispheres and Earth System (FDOMES) and Physical Oceanography Laboratory/Key Laboratory of Ocean Observation and Information of Hainan Province, Sanya Oceanographic Institution, Ocean University of China, Qingdao/Sanya, China.

[2] Laoshan Laboratory, Qingdao, China.

[3]Academy of Future Ocean, Ocean University of China, Qingdao, China.

[*] Corresponding author: Zhiwei Zhang (email: zzw330@ouc.edu.cn)

Key points:

- Submesoscales in the Kuroshio Loop Current (KLC) are examined using high-resolution simulation outputs.
- Energy exchange between submesoscales and KLC plays an important role in the local energy budget.
- Horizontal salt and heat transports by submesoscales are much larger than those by KLC eddy shedding.

Abstract

The Kuroshio Loop Current (KLC) is an important form of Kuroshio intrusion into the northeastern South China Sea (NESCS), which has significant influences on dynamical and biogeochemical processes in the NESCS. Recent studies suggested that the KLC is a hot spot of submesoscale processes (submesoscales) with spatiotemporal scales of $O(1–10)$ km and $O(1–10)$ days, but submesoscales' roles in energy cascade and salt and heat transports remain obscure. Here, we investigate this issue through analyzing outputs from a 1/48° simulation. The kinetic energy exchange rate between submesoscale and larger-scale processes (KER) is overall positive in the KLC region, which suggests the dominance of forward cascade. The magnitude of KER is comparable with the temporal change rate of larger-scale kinetic energy in the upper 200 m. We also find that magnitude and direction of KER are closely associated with strain rate and horizontal divergence of background flows, respectively. In addition, the KLC region shows elevated submesoscale salinity and heat diffusivities with magnitudes reaching $O(10^2)$ m^2s^{-1}. During the KLC period, horizontal mixing by submesoscales can transport 0.90×10^{13} kg salt and 0.71×10^{20} J heat westward into the NESCS interior, which are an order of magnitude larger than those caused by the KLC eddy shedding. These results suggest that submesoscales play important roles not only in energy cascade but also in salt and heat transports in the KLC region. Therefore, the roles of submesoscales should be taken into account when studying energy, salt, and heat budgets in the NESCS.

Plain Language Summary

As the western boundary current of the North Pacific subtropical gyre, the Kuroshio can intrude into the northeastern South China Sea (NESCS) in the form of Kuroshio Loop Current (KLC), which modulate the tracer and energy budgets of NESCS through shedding eddies. Although previous studies have reported that the KLC region is abundant with submesoscale processes (submesoscales) with spatiotemporal scales of O(1–10) km and O(1–10) days, their roles in cross-scale energy transfer and salt and heat transports are poorly known. In this study, the above issues are examined through an analysis of outputs from a 1/48° ocean simulation. We find that larger-scale processes in this region generally feed submesoscales through a forward energy transfer in upper 200 m, whose rate is comparable in magnitude with the temporal change rate of larger-scale kinetic energy. Furthermore, the horizontal mixing effect of submesoscales can transport a huge amount of heat and salt westward into the NESCS interior during the KLC period. The salt and heat transports are an order of magnitude larger than those caused by the KLC eddy shedding. The above results suggest that submesoscales associated with the KLC play important roles in the energy, heat, and salt budgets in the NESCS.

1 Introduction

Oceanic submesoscale processes (submesoscales hereafter) typically refer to the dynamic processes with spatial and temporal scales of *O*(1–10 km) and *O*(1–10 days), respectively (McWilliams, 2016; Thomas et al., 2008). Dynamically, submesoscales are characterized by order one Rossby numbers (*Ro*) and correspondingly, they can break the constrain of geostrophic balance and thus generate strong vertical motions (Mahadevan & Tandon, 2006; Yu et al., 2019; Zhang Z. et al., 2021). As a result, submesoscales can cause large vertical transports of heat, salt, oxygen, nutrients, and other tracers in the upper ocean, through which they significantly modulate both the dynamical and biogeochemical processes therein (Mahadevan et al., 2012; Mahadevan, 2016; Su Z. et al., 2018; Thompson et al., 2016). In addition, because of their mediate spatiotemporal scale and strong ageostrophic nature, submesoscales are demonstrated to behave as an important conduit connecting the oceanic balanced and unbalanced motions. Therefore, they play an irreplaceable role in the oceanic energy cascade that maintains the balance of ocean energy reservoir (Capet et al., 2008; D'Asaro et al., 2011; Gula et al., 2016; Qiu et al., 2022; Zhang Z. et al., 2023).

The South China Sea (SCS) is the largest marginal sea of the northwestern Pacific, which is linked to the northwestern Pacific through the Luzon Strait (Figure 1a). Due to the intrusion of the Kuroshio, strong monsoon winds, and complex topography, the SCS is abundant with rich multi-scale dynamic processes, including large scale circulation (Gan et al., 2016; Su J., 2004), mesoscale eddies (Wang, 2003;

Zhang Z. et al., 2016, 2017), small-scale internal waves (Alford et al., 2015; Huang et al., 2016), and microscale turbulent mixing (Tian et al., 2009; Yang et al., 2016). Both recent observation and simulation studies have revealed that submesoscales in the SCS are also very active (e.g., Cao et al., 2022; Dong & Zhong, 2018; Li et al., 2019; Lin et al., 2020; Zhang J. et al., 2021; Zhang X. et al., 2022; Zhang Z. et al., 2020; Zhong et al., 2017). Given the potential importance of submesoscales to material transport, energy cascade, and biogeochemical processes in the SCS, they have received more and more attentions in recent years.

When the nascent Kuroshio flows northward through the Luzon Strait, its main axis often bends clockwise and intrudes into the northeastern SCS (NESCS) in the form of the Kuroshio Loop Current (KLC) in winter (Shaw, 1989; Sheremet, 2001; Sun et al., 2020; Figure 1a). As the KLC develops, it can finally shed an anticyclonic mesoscale eddy in the NESCS, which can further induce a cyclonic mesoscale eddy in the trailing (Zhang Z. et al., 2017). The anticyclonic eddy shedding from the KLC can transport a considerable amount of warmer, saltier, and oligotrophic Kuroshio water into the NESCS that significantly modulate the tracer budgets therein (Zhang Z. et al., 2017). Recently, through analyzing submesoscale permitting simulation outputs, the study of Zhang Z. et al. (2020) have pointed out that the KLC region is a hotspot of submesoscales. These submesoscales are suggested to be generated by the combination of mixed-layer baroclinic instability and strain-induced frontogenesis. The authors further argued that after generation, the submesoscales may transfer part of their kinetic energy (KE) inversely to mesoscale eddies. The above simulation results have been to a large degree verified by Zhang J. et al. (2021) based on the analysis of long-term moored observations. Besides, the most recent observation study of Zhang X. et al. (2022) have revealed that interactions between the KLC and the complex topography in the Luzon Strait and the region southwest of Taiwan can generate submesoscale coherent vortices, which means the occurrence of forward energy cascade.

Although submesoscales in the NESCS (the KLC region in particular) have been investigated by a couple of studies, the following two issues remain to be revealed. First, the spatiotemporal characteristics of submesoscale energy cascade and its role in modulating the KLC are still obscure. Second, during the development or steady stage of the KLC (before the eddy shedding), whether and to what degree can the horizontal mixing effect of the submesoscales surrounding the KLC contribute to the NESCS-Pacific water exchange remain unknown. Here, these two scientific issues are explored by an analysis of the outputs from a submesoscale permitting simulation (~2-km resolution). The remainder of the paper is organized as follows. Section 2 describes the data and methods. Section 3 shows general characteristics of the KLC and submesoscales in the study region. Section 4 reveals the energy cascade (refers only to KE cascade hereafter) associated with submesoscales. In section 5, the salt and heat transports caused by submesoscales are quantitatively evaluated. Finally, summary and discussion of the study are given in section 6.

2 Data and methods

2.1 High-resolution simulation outputs

The outputs from the MITgcm (Massachusetts Institute of Technology General Circulation Model) LLC4320 simulation were used in this study to investigate the energy cascade and salt transport associated with submesoscales. The LLC4320 simulation is forced by the 6-hourly ECMWF (European Centre for Medium-Range Weather Forecasts) atmospheric analysis as well as the 16 main tidal components. Horizontally, it has a 1/48° (~2 km) resolution and in the vertical, it contains 90 layers whose resolution ranges from 1 to 20 m in the upper 200 m (focus of this study). The time range of LLC4320 is from September 13, 2011 to November 14, 2012 (14 months) and the outputs are stored with an hourly interval. With an effective resolution of ~10 km, the LLC4320 simulation can, to a certain degree, resolve submesoscales at the low and mid latitudes, particularly the larger ones generated by mixed-layer baroclinic instabilities (Dong et al., 2020).

Until now, the LLC4320 simulation has been used by a number of studies to investigate the submesoscales in both global and regional scopes (e.g., Miao et al., 2021; Qiu et al., 2018; Rocha et al., 2016; Su Z. et al., 2018; Zhang Z. et al., 2023). Recently, the LLC4320 data was also applied to submesoscale researches in the SCS, and its performance has been validated by multiple in situ observations (Cao et al., 2019; Lin et al., 2020). Here, hourly LLC4320 data in the NESCS are extracted and analyzed (115–123°E, 17–24°N; red box in Figure 1a). In order to remove the tidal and inertial signals, the hourly data were firstly 48-hour low-pass filtered (fourth-order Butterworth) and then averaged on a daily basis.

In Figures 1b–c, we compare the mean sea surface height (SSH) and surface geostrophic currents in winter (i.e., December, January, and February) from the LLC4320 data with those from the altimeter data. Here, the altimeter data are the multiple-satellite-merged gridded products from AVISO with temporal and spatial resolutions of 1 day and 1/4°, respectively. Given that the free run LLC4320 simulation cannot reproduce the real KLC in the same period (i.e., 2011–2012), the climatologically winter mean altimeter data during the strong KLC periods between 1999–2000, 2011–2012, 2016–2017, and 2017–2018 (Sun et al., 2020) are used for comparison. It reveals that both the LLC4320 and altimeter SSHs (and surface geostrophic currents) display an evident KLC in the NESCS in winter. The KLC pattern in the LLC4320 is overall similar to the altimeter result, although its size and strength are slightly weaker. The reasonable simulation of the KLC in the LLC4320 lays the basis to perform the analysis in this study.

2.2 Method of scale separation

In this study, a period 15 days was used as the separation time scale between submesoscales and meso- to large-scale processes. Specifically, we obtained the meso- to large-scale (larger-scale for short hereafter) and submesoscale signals by performing the 15-day low-pass and high-pass filters to the subinertial LLC4320 daily data, respectively. The 15-day separation scale was chosen because the recent observations from a submesoscale mooring array have suggested that the subinertial velocity and temperature anomalies (with periods shorter than 15 days) are closely related to the submesoscales with large Rossby number and vertical velocity (Zhang Z.

et al., 2021). The temporal separations were used rather than spatial scale because spatial filters can result in large errors near the topography (e.g., coast and islands). More recently, through analysing high-resolution simulation data in the NESCS, Zhang J. et al. (2021) found a good statistical consistency between the submesoscale quantities calculated from 15-day temporal and 80-km spatial high-pass filters. Therefore, we finally choose 1–15 days time scale to define submesoscales in the NESCS.

2.3 Kinetic energy exchange rate

In this study, the coarse-graining approach was adopted to calculate the KE exchange rate (KER hereafter) between the submesoscales and larger-scale processes. Coarse-graining approach was early established to deal with turbulence problems (Eyink, 2005; Germano, 1992; Leonard, 1975) and recently, it has been successfully applied to investigate oceanic energy cascade issues based on both simulation and observation data (e.g., Aluie et al., 2018; Naveira Garabato et al., 2022; Schubert et al., 2020; Srinivasan et al., 2022). The advantage of coarse-graining approach is that its calculation is not affected by statistical homogeneity or isotropy assumption adopted in the traditional turbulence theory (Aluie et al., 2018). The KER in the coarse-graining approach is defined as

$$KER = -\left[(\overline{uu} - \bar{u}\,\bar{u})\bar{u}_x + (\overline{uv} - \bar{u}\,\bar{v})(\bar{u}_y + \bar{v}_x) + (\overline{vv} - \bar{v}\,\bar{v})\bar{v}_y\right] - \left[(\overline{uw} - \bar{u}\,\bar{w})\bar{u}_z + (\overline{vw} - \bar{v}\,\bar{w})\bar{v}_z\right]. \quad (1)$$

In Eq. (1), u, v, and w are zonal, meridional, and vertical velocity, respectively; Overbar denotes a larger-scale average; Subscripts x, y, and z denote zonal, meridional, and vertical partial derivatives, respectively. The first and second right-hand terms represent the horizontal energy flux and vertical energy flux, respectively. Physically, KER represents the KE exchange between scales finer and coarser than a certain scale, whose positive and negative values represent forward and inverse energy cascade, respectively. Here, the 15-day separation scale was used to calculate the KER between larger-scale processes and submesoscales (see section 2.2). Given that in the upper 200 m layer where submesoscales are active, the vertical energy flux is one order of magnitude smaller than the horizontal energy flux (Figure S1), only the horizontal term of the KER was finally analyzed in the study.

2.4 Submesoscale salt and heat fluxes and diffusivities

The submesoscale salt flux ($\boldsymbol{SF}$) on each isopycnal is calculated using

$$\boldsymbol{SF} = \overline{\boldsymbol{u}'S'}. \qquad (2)$$

where overbar denotes 15-day running mean, and $\boldsymbol{u}'$ and S' denote velocity and salinity anomalies caused by submesoscales on each specific isopycnal, respectively. After obtaining the $\boldsymbol{SF}$ vector, we further decomposed it into a rotational component and a divergent component using Helmholtz decomposition (e.g., Jayne & Marotzke, 2002). For a specific region with scale much larger than submesoscales, the rotational component of $\boldsymbol{SF}$ transports as much salt to this region as it does out of that region. As a result, it plays no role in the salt budget in this region. Given that it is the divergent component of $\boldsymbol{SF}$ ($\boldsymbol{SF_D}$) that eventually determines the salinity budget, we only focus on the $\boldsymbol{SF_D}$ in this study. Based on the $\boldsymbol{SF_D}$, we then calculated the isopycnal submesoscale salt diffusivity K_S using

$$K_S = -\boldsymbol{SF_D} \cdot \nabla \overline{S} / \left|\nabla \overline{S}\right|^2 . \qquad (3)$$

where $\nabla \overline{S}$ is the larger-scale salinity gradient.

In order to evaluate the role of submesoscales in salt transport, we calculated the submesoscale salt transport per unit depth (STD) across the Kuroshio main axis (Ku) using

$$\mathrm{STD} = \int_{Ku} \boldsymbol{SF_D} \cdot \boldsymbol{n}\, dl . \qquad (4)$$

Here, $\boldsymbol{n}$ represents the normal unit vector of dl and the integration is along the Ku, which is defined as the SSH contour with the highest average salinity at 150 m where the vertical salinity maximum occurs. Based on STD, we can further calculate the vertically integrated salt transport (IST) across the Ku using

$$\mathrm{IST} = \int_{-D_\sigma}^{0} \mathrm{STD}\, dz . \qquad (5)$$

D_σ is the depth of the $24.3\sigma_0$ isopycnal (approximately 150–200 m in the KLC region), below which the influence of submesoscales is negligible. Because we only focus on the salt transport across the Luzon Strait, the part of Ku east of 120.8 °E (solid orange line in Figure 1a) is not taken into account.

Similarly, we can also calculate the submesoscale heat flux ($\boldsymbol{HF}$) on each isopycnal using

$$\boldsymbol{HF} = \rho_0 C_p \overline{\boldsymbol{u}'\theta'} . \qquad (6)$$

Here, θ' denotes potential temperature anomalies caused by submesoscales on each specific isopycnal, $\rho_0 = 1025\ kg/m^3$ is the referenced density, and $C_p = 3997\ J/({}^oC \cdot kg)$ is the thermal capacity. Through replacing salinity with potential temperature in Eq. (3–5), we can obtain isopycnal submesoscale heat diffusivity K_θ, submesoscale heat transport per unit depth (HTD), and vertically integrated heat transport (IHT).

3 General features of the KLC and submesoscales

In Figure 2, we show the distributions of the simulated surface Rossby number (*Ro*) calculated using $Ro = \zeta / f$, where $\zeta = v_x - u_y$ is the relative vorticity and *f* is the planetary vorticity. It clearly shows that when the northward-flowing Kuroshio passes by the Luzon Strait, it bends clockwise to form the KLC in the region southwest of Taiwan. The KLC began forming in late December 2011, reached maturity in February and March 2012, and gradually decayed until its disappearance in early May. Corresponding to the strong anticyclonic currents of the KLC, it shows nearly universal negative *Ro* within its core. The large values of *Ro* occur at the periphery of the KLC, whose magnitudes reach order one. The distributions of the large *Ro* values manifest as elongated filaments, fronts, and coherent vortices, indicating the occurrence of submesoscales.

In Figures 3a and 3b, we compare the depth-time distributions of the larger-scale and submesoscale KE averaged over the KLC region (i.e., the pink solid box in Figure 2c). Corresponding to the occurrence of the KLC between late December 2011 and early May 2012, the larger-scale KE was significantly elevated throughout the upper 200 m (Figure 3a). Although the KE of the KLC is surface intensified, its influence depth can reach 200 m. Actually, recent moored observations revealed that velocity signals of the KLC can penetrate to as deep as 2000 m in the

NESCS (Sun et al., 2020). The submesoscale KE overall has a good correspondence with the larger-scale KE, which showed elevated values during the KLC period between January to April 2012 (purple box in Figures 3b–c). Compared with the larger-scale KE, the submesoscale KE decreases more rapidly with depth and its magnitude is one order of magnitude smaller. Similar to the submesoscale KE, the root-mean-squared *Ro* (RMS-*Ro*) of submesoscales was also elevated during the KLC period, whose magnitude reached 0.2–0.3 at the sea surface.

Mixed-layer depth (MLD) and strain rate of background flows ($\overline{\alpha} = \sqrt{(\overline{v}_y - \overline{u}_x)^2 + (\overline{v}_x + \overline{u}_y)^2}$) are key factors that determine the intensity of mixed-layer instability and strain-induced frontogenesis, respectively. In order to better understand the temporal modulations of submesoscale activities, in Figure 4, we compare the time series of upper 100-m-averaged submesoscale KE in the KLC region and region-averaged MLD and $\overline{\alpha}$. It shows that in the KLC region, the submesoscale KE is well correlated with $\overline{\alpha}$ with the Pearson correlation coefficient (R) reaching 0.46 (Figure 4a; R = 0.094 for the 95% confidence level). With respect to the MLD, however, it is weakly correlated with the submesoscale KE at the intra-seasonal time scale with R = 0.14 (Figure 4b). This is different from previous results found in open oceans that submesoscale quantities have good correlations with MLD at the seasonal time scale corresponding to the seasonal modulation of mixed-layer instability (e.g., Dong et al., 2020; Puzina et al., 2021; Thompson et al., 2016; Yu et al., 2019). The results found here suggest that submesoscales in the KLC may primarily be generated by strain-induced frontogenesis while the role of mixed-layer instability may be secondary. To test the sensitivity of the above correlations regarding the time and area averages, we change the averaging window of the time series to 5 and 20 days and change the averaging area to a smaller KLC region (purple dashed box in Figure 2c). The results show that the values of *R* only have slight changes and they were not sensitive to the slight changes of time and space averaging windows (Figures S2 and S3).

Regarding the submesoscales in the KLC region, there are two things that deserve to be noted. First, strong submesoscales also occurred in early and mid December 2011, although the KLC did not form yet (Figures 2a and 3b–c). During that period, the MLD quickly deepened due to ocean's heat loss to atmosphere (Figure 3), which means quick accumulation of available potential energy within the mixed layer. Therefore, the strong submesoscales in December were likely generated by enhanced mixed-layer instability at that time (Boccaletti et al., 2007; Callies et al., 2016). Second, although the strength of submeoscales decreases rapidly with depth, their influence depth can reach 100 m, which is larger than the MLD (i.e., maximum of 50 m in winter). This phenomenon is consistent with recent submesoscale resolving in situ observations (e.g., Yu et al., 2019; Zhang Z., 2021).

4 Energy cascade associated with submesoscales

4.1 Spatiotemporal characteristics of submesoscale energy cascade

In order to study submesoscale energy cascade in the KLC region, we calculated the KER using the coarse-graining approach (section 2.3). From the spatiotemporal variations of KER in Figure 5, we find that the KLC and the path of Kuroshio in the Luzon Strait and east of Taiwan are hotspots of submesoscale energy cascade, where the magnitude of KER reaches $O(10^{-6}–10^{-5})$ $m^2·s^{-3}$. Along the path of the Kuroshio in the Luzon Strait and east of Taiwan, the KER is mainly positive, indicating the dominance of forward energy cascade. With respect to the KLC region, although the region-averaged KER is overall positive (Figure 6), its sign and magnitude are highly non-uniform in aspects of both space and time. Specifically, at the periphery of the KLC (i.e., along its axis), the KER tends to be positive most of the time. Within the core of the KLC, the KER was primarily positive in the growth period of KLC in January but negative values (i.e., inverse cascade) became more evident during the mature period of KLC, particularly in March.

To evaluate the role of KER in the energy budget and thus evolution of KLC, we compare the region-averaged KER in the KLC region with the material derivative of the larger-scale KE (i.e., DKE/Dt) therein (Figures 6 and 7). The upper 100 m-averaged time series of DKE/Dt in the KLC region shows significant intra-seasonal variations with period of 10–20 days (Figure 6). At the intra-seasonal time scale, the DKE/Dt is negatively correlated with the KER with R of -0.39 (R = -0.18 for the 95% confidence level). For the positive and negative values of KER, they mostly correspond to decrease and increase of larger-scale KE, respectively. As a result, the composite mean profile of DKE/Dt during the periods of positive (negative) KER is negative (positive) throughout the upper 200 m (Figure 7). If the upper 200 m is considered, the ratios between the RMS values of KER and DKE/Dt during the periods of positive and negative KER reach 0.66 and 0.50, respectively. The above results demonstrate that submesoscale energy cascade is a leading order process in the energy budget of the larger-scale KE in the KLC region. In another word, submesoscales can significantly modulate the intra-seasonal variation of KLC through direct or inverse energy cascade. Sensitivity analysis shows that the above correlations are also insensitive to the slight changes of time and space averaging windows (Figures S4 and S5).

4.2 Roles of strain and divergence

The recent study of Srinivasan et al. (2022) suggested that horizontal divergence ($\bar{\delta} = \bar{u}_x + \bar{v}_y$) and $\bar{\alpha}$ (i.e., strain rate) of background flows are two important factors that determine submesoscale energy cascade (i.e., KER). In order to understand the roles of $\bar{\delta}$ and $\bar{\alpha}$, we compare their mean spatial distributions in March 2012 with the corresponding KER at the 5-m depth (Figures 8a–c). It shows that except for the vicinity of islands, large values of $\bar{\alpha}$ mainly occur at the periphery of KLC. Although the sign of KER seems independent of the $\bar{\alpha}$, their magnitudes have similar spatial distributions in the KLC region. That is to say, large magnitudes of KER tend to occur in regions with strong strain field. By comparing KER with $\bar{\delta}$, we find that the forward (inverse) energy cascade occurs more frequently in regions with flow convergence (divergence). These results suggest that the strength and direction of submesoscale energy cascade depend on $\bar{\alpha}$ and $\bar{\delta}$, respectively. In order to verify the above phenomenon, we further calculate the spatial correlations between the KER and $\bar{\delta}/|\bar{\delta}| \times \bar{\alpha}$ using all of the grid points in the KLC region (Figure 8d). During the KLC period, the *R* is nearly always negative, its values are generally between -0.45 and -0.15 (except for mid April). The mean value of *R* is -0.28, which far exceeds the 95% confidence level (i.e., *R* = -0.014). Similar results also apply to other depths in the upper 200 m (Figure S6) except that the *R* is slightly smaller than that at near surface. Therefore, the quantity $\bar{\delta}/|\bar{\delta}| \times \bar{\alpha}$ is a useful indicator that can be used to judge the magnitude and sign of submesoscale energy cascade.

5 Salt and heat transports by submesoscales

Previous studies demonstrated that the anticyclonic eddy shedding from KLC could transport a huge amount of warm and salty water into the NESCS interior within a short time (e.g., Zhang et al., 2017). However, by this warm and salty water transport mechanism, no heat nor salt will enter the NESCS interior in absence of eddy shedding from the KLC. Given that the KLC behaves as a mesoscale salt and temperature filament, and that there are energetic submesoscales at the periphery of KLC, it is theoretically expected that submesoscales can contribute to the salt and heat transports into the NESCS through the horizontal mixing effect. In this section, the roles of submesoscales in the salt and heat fluxes as well as the corresponding westward transports across the Luzon Strait are quantitatively evaluated.

5.1 Submesoscale salt and heat fluxes and diffusivities

Before discussing submesoscales-induced salt and heat fluxes, we first examine the characteristics of KLC water (i.e., water within the KLC) by comparing its mean temperature-salinity (*T*-*S*) diagram with that of the typical Kuroshio water and the NESCS water (Figure 9). The significant difference between the NESCS water and the Kuroshio water is that the latter is warmer and saltier in the upper layer above $25.55\sigma_0$ (mean depth at ~250 m) but colder and fresher below that. For the Kuroshio water, the maximum temperature and salinity can reach 26.7 °C and 34.75 g/kg, respectively, while the respective values for the NESCS water are only 26 °C and 34.55 g/kg. In the upper layer, the mean *T*-*S* property of the KLC water is between the Kuroshio water and NESCS water. At the KLC edge, the *T*-*S* properties are close to the Kuroshio water but the temperature and salinity are slightly lower on the same isopycnals. Here, the KLC edge is defined as the SSH contour with the highest average salinity at 150 m (i.e., the main axis of KLC), where the vertical salinity maximum occurs. As we will discuss below, the slightly lower temperature and salinity at the KLC edge is associated with the isopycnal mixing or tracer transport caused by submesoscales.

Based on the method in section 2.4, we calculate the divergent component of the isopycnal salt flux induced by submesoscales ($\boldsymbol{SF_D}$). In Figure 10, we show the spatial distributions of salinity and $\boldsymbol{SF_D}$ on the $23.5\sigma_0$ isopycnal (i.e., at depth of 120–150 m) at different KLC stages. It shows that the KLC edge behaves like a salty mesoscale filament that is saltier than the waters inside and outside of the KLC, which is consistent with the result in Figure 9. Due to the combination of large salinity gradient and energetic submesoscales, it shows large down-gradient $\boldsymbol{SF_D}$ at the KLC filament. The magnitude of $|\boldsymbol{SF_D}|$ reaches up to $O(10^{-2})$ g/kg·m/s, which is overall two orders of magnitude larger than that in absence of KLC (Figure S7). The large values of $|\boldsymbol{SF_D}|$ mainly occur in the southern and western part of the KLC filament where salinity gradient is strong. Corresponding to the opposite salinity gradient at the two sides of the KLC filament, direction of the $\boldsymbol{SF_D}$ is mainly southwestward at the outer but northeastward at the inner side of the KLC's southwestern edge. Due to the large down-gradient $\boldsymbol{SF_D}$ associated with submesoscales, the water at the KLC edge gradually becomes fresher along its flowing direction. It is also found that after the Kuroshio flows out of the NESCS and reaches east of Taiwan, its salinity becomes much lower than that east of Luzon. This salinity reduction along the Kuroshio path becomes less evident during the leaping-path period of Kuroshio (Figure S7). The submesoscales also induce elevated and down-gradient $\boldsymbol{HF_D}$ at the KLC edge whose magnitude reaches $O(10^4)$ W/m^2 (Figure S8). The spatial distribution of $\boldsymbol{HF_D}$ is very similar to the $\boldsymbol{SF_D}$, which is understandable because of the temperature-salinity compensation on the isopycnal. During the Kuroshio leaping-path period, the $|\boldsymbol{HF_D}|$ is also significantly weakened (Figure S9). The above results suggest that submesoscales at the KLC not only take warmer and saltier Kuroshio water into the NESCS but also significantly modulate the water property of Kuroshio through isopycnal mixing.

Based on Eq. (3) in section 2.4, we calculate the 15-day averaged submesoscale salt diffusivity K_S whose time-dependent spatial distributions are shown in Figure 11. We find that the K_S is strongly inhomogeneous in aspect of spatial distribution. The large values of K_S primarily occur in the KLC region where submesoscales are active. Corresponding to the down-gradient $\boldsymbol{SF_D}$, the K_S is dominantly positive at the KLC edge. Its magnitude there reaches $O(10^2)$ m^2/s, which is 1–2 orders of magnitude larger than that in the NESCS interior. Although negative values of K_S also occur, particularly in the interior area of the KLC, their magnitude is overall smaller than the positive ones (i.e., smaller than 100 m^2/s). The submesoscale heat diffusivity K_θ also reaches $O(10^2)$ m^2/s at the KLC edge, and both its magnitude and spatial distribution are overall similar to K_S (Figure S10).

5.2 Submesoscales-induced salt and heat transports

Based on the method in section 2.4, we calculated the submesoscale salt and heat transports across the KLC main axis. The mean vertical profile of submesoscale salt and heat transports per unit depth (i.e., STD and HTD) during the maturity period of KLC (i.e., March, 2012) is shown in Figure 12a. Both the salt and heat transports are from the KLC to the NESCS (i.e., positive values) throughout the upper 200 m, whose magnitudes are of $O(10^4)$ g/kg·m^2/s and $O(10^{11})$ W/m/s, respectively. Although submesoscales are generally surface intensified, the maximum submesoscale salt transport occurs at 50 m with magnitude reaching 5.3×10^4 g/kg·m^2/s, which is 26 times larger than that at sea surface (i.e., 0.2×10^4 g/kg·m^2/s). Similar to the vertical structure of the STD, the HTD is also subsurface intensified, but the maximum value of HTD appears at a deeper depth (i.e., 90 m).

Different from the salt and heat transports, the mean K_S and K_θ at the KLC main axis are surface intensified, whose magnitudes sharply decrease from ~450 m^2/s at surface to ~250 m^2/s at 50 m depth. In the layer between 50–200 m the K_S and K_θ are overall between 100 and 250 m^2/s. The difference between submesoscale salt/heat transport and diffusivity is understandable because the former not only depends on diffusivity but also depends on the horizontal salt/heat gradient, which is subsurface intensified in the KLC region. Note that submesoscale salt/heat transport also exists in the leaping-path stage of Kuroshio (i.e., non-KLC periods) in the Luzon Strait, although its magnitude is smaller (Figures S7 and S9).

In Figure 13, we show the time series of the vertically integrated submesoscale salt transport (IST) and heat transport (IHT) across the Ku near the Luzon Strait (including both KLC and non-KLC periods). We find that the IST and IHT are predominately positive throughout the year, which suggests down-gradient salt and heat transports from the Kuroshio into the NESCS. The IST and IHT were significantly enhanced during the main KLC period between January and April, 2012 and their magnitudes were largest in March 2012 when the KLC was at its mature stage. The time-mean IST during the KLC period reached 1.78×10^6 g/kg·m^3/s, which is 370% larger than the mean value during the non-KLC period (3.80×10^5 g/kg·m^3/s). Meanwhile, the time-mean IHT during the KLC period is 240% of that during non-KLC periods (8.65×10^{12} W vs. 2.56×10^{12} W). The larger IST and IHT during the KLC period are attributed to the combination of stronger submesoscales and longer integral along the Ku.

We need to note that the lifespan of the simulated KLC by the LLC4320 is longer than the true KLCs observed by altimeter data, which has a mean lifespan of ~57 days (Zhang Z. et al., 2017; Sun et al., 2020). If we multiply the simulation-derived mean IST and IHT during the KLC period by the 57-day period (i.e., the mean lifespan of KLCs in the real ocean), we can roughly estimate that submesoscales associated with a KLC event can transport 0.90×10^{13} kg salt and 0.71×10^{20} J heat into the NESCS. Zhang et al. (2017) analyzed the radius and temperature/salinity anomaly of the anticyclonic eddy shedding from the KLC based on the observation. According to the observational study, we can estimate that in terms of annual mean, the KLC eddy shedding can transport 1.90×10^{12} kg salt and 2.08×10^{19} J heat into the NESCS, which are an order smaller than that associated with submesoscale IST and IHT during the KLC period, respectively. If the non-KLC period is also considered, we can roughly estimate that the westward salt and heat transports caused by submesoscales throughout the year (between October 1th, 2011 and September 30th, 2012) are as high as 2.77×10^{13} kg and 1.69×10^{21} J, respectively. The above results demonstrate that when the Kuroshio is at the loop or leaping state (excluding leaking intrusion state), horizontal mixing effect of submesoscales is the dominant salt and heat transports mechanism from the Kuroshio to the NESCS while the role of KLC eddy shedding is secondary. Note that the above heat and salt transport values are very rough estimates, which need to be confirmed by high-resolution in situ observations in the future.

6 Summary and discussion

In this study, outputs of the 1/48° LLC4320 simulation were used to investigate energy cascade and salt transport associated with submesoscales in the KLC region of the NESCS. The simulation results show that active submesoscales with $O(1)$ *Ro* occurred in the upper 200 m in the KLC between January and April 2012. The simulated submesoscale KE in the KLC region is well correlated with the background strain rate ($\bar{\alpha}$) but poorly correlated with MLD, which suggests strain-induced frontogenesis may play a more important role than mixed-layer instability in the generations of these submesoscales during the KLC period.

The KLC region is a hotspot of submesoscale energy cascade with elevated KER values compared with other regions in the NESCS. Overall, KER is dominated by positive values or forward energy cascade in the KLC region, particularly along the main axis of KLC. In the interior area of KLC, however, inverse energy cascade becomes evident at the growth stage of KLC. The ratio between KER and material derivative of the larger-scale KE exceeds 0.5 in the upper 200 m and their time series have a good correlation, demonstrating that submesoscale energy cascade plays an important role in modulating the energy budget and thus evolution of KLC. We also find that the sign and magnitude of KER are to a large degree associated with the horizontal divergence ($\bar{\delta}$) and $\bar{\alpha}$, respectively. As a result, KER has a significantly negative correlation with the parameter $\bar{\delta}/|\bar{\delta}| \times \bar{\alpha}$, which provides a great index to infer submesoscale energy cascade from larger-scale current velocity in the future.

The active submesoscales in the KLC region result in large down-gradient salt and heat fluxes (i.e., $\boldsymbol{SF_D}$ and $\boldsymbol{HF_D}$) and positive horizontal diffusivities (i.e., K_S and K_θ). At the KLC edge, magnitudes of $\boldsymbol{SF_D}$ and $\boldsymbol{HF_D}$ reach $O(10^{-2})$ m/s and

$O(10^4)$ W/m^2, respectively, which are 1–2 orders larger than those in the NESCS interior and those during the non-KLC period. Corresponding to the down-gradient $\boldsymbol{SF_D}$ and $\boldsymbol{HF_D}$, the K_S and K_θ are overall positive at the KLC edge with values reaching $O(10^2)$ m^2/s. If the real lifespan of KLC is considered, the submesoscale $\boldsymbol{SF_D}$ and $\boldsymbol{HF_D}$ associated with a KLC event can roughly transport 0.90×10^{13} kg salt and 0.71×10^{20} J heat into the NESCS, respectively. The above values are one order larger than the equivalent salt and heat transports caused by KLC eddy shedding (Zhang et al., 2017). When the non-KLC period is also included, westward salt and heat transports induced by submesoscales throughout the year reach 2.77×10^{13} kg and 1.69×10^{21} J, respectively. The above findings demonstrate that when the Kuroshio is at the loop or leaping state, horizontal mixing effect of submesoscales is the dominant mechanism for salt and heat transports from the Kuroshio to the NESCS.

This study reveals that the KLC can induce active submesoscales in the NESCS. Interactions between submesoscales and KLC significantly modulate the variations of KLC in terms of energetics. In addition, the horizontal mixing effect of submesoscales can indeed transport a huge amount of salt and heat from the Kuroshio into the NESCS. It suggests that in addition to the well-known KLC itself, the active submesoscales induced by KLC also significantly modulate the energy, salt, and heat budgets in the NESCS. Given that the KLC has distinct seasonal-to-decadal variations (e.g., Sun et al., 2020), how it will modulate the temporal variations of submesoscales and how these submesoscales further modulate the low-frequency variations of energy and salt budget in the NESCS also deserves to be studied in the future. We should acknowledge that the analysis in this study mainly relies on the submesoscale permitting simulation (with resolution of ~2 km), the quantitative roles of submesoscales in the energy and salt budget issues in the NESCS need to be examined in the future based on submesoscale resolving observations.

Acknowledgments

This study is jointly supported by the National Natural Science Foundation of China (42222601, 42076004, 92258301, 62206015) and the National Key Research and Development Program of China (2022YFC3105003). Z. Z. is also supported by the "Taishan" Talents program (tsqn202103032) and Shandong Provincial Natural Science Foundation (ZR2023JQ013).

Open Research

The LLC4320 is available at https://data.nas.nasa.gov/ecco/data.php. The altimeter data were downloaded from https://cds.climate.copernicus.eu/cdsapp#!/search?text=aviso.

References

Alford, M. H., Peacock, T., MacKinnon, J. A., Nash, J. D., Buijsman, M. C., Centurioni, L. R., et al. (2015). The formation and fate of internal waves in the South China Sea. *Nature*, *521*(7550), 65–69. https://doi.org/10.1038/nature14399

Aluie, H., Hecht, M., & Vallis, G. K. (2018). Mapping the Energy Cascade in the North Atlantic Ocean: The Coarse-Graining Approach. *Journal of Physical Oceanography*, *48*(2), 225–244. https://doi.org/10.1175/JPO-D-17-0100.1

Boccaletti, G., Ferrari, R., & Fox-Kemper, B. (2007). Mixed Layer Instabilities and Restratification. *Journal of Physical Oceanography*, *37*(9), 2228–2250. https://doi.org/10.1175/JPO3101.1

Callies, J., Flierl, G., Ferrari, R., & Fox-Kemper, B. (2016). The role of mixed-layer instabilities in submesoscale turbulence. *Journal of Fluid Mechanics*, *788*, 5–41. https://doi.org/10.1017/jfm.2015.700

Cao, H., Jing, Z., Fox-Kemper, B., Yan, T., & Qi, Y. (2019). Scale Transition From Geostrophic Motions to Internal Waves in the Northern South China Sea. *Journal of Geophysical Research: Oceans*, *124*(12), 9364–9383. https://doi.org/10.1029/2019JC015575

Cao, H., Meng, X., Jing, Z., & Yang, X. (2022). High-resolution simulation of upper-ocean submesoscale variability in the South China Sea:Spatial and seasonal dynamical regimes. *Acta Oceanologica Sinica*, *41*(7), 26–41. https://doi.org/0.1007/s13131-022-2014-4

Capet, X., McWilliams, J. C., Molemaker, M. J., & Shchepetkin, A. F. (2008). Mesoscale to Submesoscale Transition in the California Current System. Part III: Energy Balance and Flux. *Journal of Physical Oceanography*, *38*(10), 2256–2269.

https://doi.org/10.1175/2008JPO3810.1

D'Asaro, E., Lee, C., Rainville, L., Harcourt, R., & Thomas, L. (2011). Enhanced Turbulence and Energy Dissipation at Ocean Fronts. *Science*, *332*(6027), 318–322. https://doi.org/10.1126/science.1201515

Dong, J., & Zhong, Y. (2018). The spatiotemporal features of submesoscale processes in the northeastern South China Sea. *Acta Oceanologica Sinica*, *37*(11), 8–18. https://doi.org/10.1007/s13131-018-1277-2

Dong, J., Fox-Kemper, B., Zhang, H., & Dong, C. (2020). The Seasonality of Submesoscale Energy Production, Content, and Cascade. *Geophysical Research Letters*, *47*(6). https://doi.org/10.1029/2020GL087388

Eyink, G. L. (2005). Locality of turbulent cascades. *Physica D: Nonlinear Phenomena*, *207*(1–2), 91–116. https://doi.org/10.1016/j.physd.2005.05.018

Gan, J., Liu, Z., & Hui, C. R. (2016). A Three-Layer Alternating Spinning Circulation in the South China Sea. *Journal of Physical Oceanography*, *46*(8), 2309–2315. https://doi.org/10.1175/JPO-D-16-0044.1

Germano, M. (1992). Turbulence: the filtering approach. *Journal of Fluid Mechanics*, *238*, 325–336. https://doi.org/10.1017/S0022112092001733

Gula, J., Molemaker, M. J., & McWilliams, J. C. (2016). Topographic generation of submesoscale centrifugal instability and energy dissipation. *Nature Communications*, *7*(1), 12811. https://doi.org/10.1038/ncomms12811

Huang, X., Chen, Z., Zhao, W., Zhang, Z., Zhou, C., Yang, Q., & Tian, J. (2016). An extreme internal solitary wave event observed in the northern South China Sea. *Scientific Reports*, *6*(1), 30041. https://doi.org/10.1038/srep30041

Jayne, S. R., & Marotzke, J. (2002). The Oceanic Eddy Heat Transport. *Journal of Physical Oceanography*, *32*(12), 3328–3345. https://doi.org/10.1175/1520-0485(2002)032<3328:TOEHT>2.0.CO;2

Leonard, A. (1975). Energy Cascade in Large-Eddy Simulations of Turbulent Fluid Flows. In *Advances in Geophysics* (Vol. 18, pp. 237–248). Elsevier. https://doi.org/10.1016/S0065-2687(08)60464-1

Li, J., Dong, J., Yang, Q., & Zhang, X. (2019). Spatial-temporal variability of submesoscale currents in the South China Sea. *Journal of Oceanology and Limnology*, *37*(2), 474–485. https://doi.org/10.1007/s00343-019-8077-1

Lin, H., Liu, Z., Hu, J., Menemenlis, D., & Huang, Y. (2020). Characterizing meso- to submesoscale features in the South China Sea. *Progress in Oceanography*, *188*, 102420. https://doi.org/10.1016/j.pocean.2020.102420

Mahadevan, A. (2016). The Impact of Submesoscale Physics on Primary Productivity of Plankton. *Annual Review of Marine Science*, *8*(1), 161–184. https://doi.org/10.1146/annurev-marine-010814-015912

Mahadevan, A., & Tandon, A. (2006). An analysis of mechanisms for submesoscale vertical motion at ocean fronts. *Ocean Modelling*, *14*(3–4), 241–256. https://doi.org/10.1016/j.ocemod.2006.05.006

Mahadevan, A., D’Asaro, E., Lee, C., & Perry, M. J. (2012). Eddy-Driven Stratification Initiates North Atlantic Spring Phytoplankton Blooms. *Science*, *337*(6090), 54–58. https://doi.org/10.1126/science.1218740

McWilliams, J. C. (2016). Submesoscale currents in the ocean. *Proceedings of the Royal Society A: Mathematical, Physical and Engineering Sciences*, *472*(2189), 20160117. https://doi.org/10.1098/rspa.2016.0117

Miao, M., Zhang, Z., Qiu, B., Liu, Z., Zhang, X., Zhou, C., et al. (2021). On Contributions of Multiscale Dynamic Processes to the Steric Height in the Northeastern South China Sea as Revealed by Moored Observations. *Geophysical Research Letters*, *48*(14). https://doi.org/10.1029/2021GL093829

Naveira Garabato, A. C. N., Yu, X., Callies, J., Barkan, R., Polzin, K. L., Frajka-Williams, E. E., et al. (2022). Kinetic Energy Transfers between Mesoscale and Submesoscale Motions in the Open Ocean's Upper Layers. *Journal of Physical Oceanography*, *52*(1), 75–97. https://doi.org/10.1175/JPO-D-21-0099.1

Puzina, O. S., Kubryakov, A. A., & Mizyuk, A. I. (2021). Seasonal and Vertical Variability of Currents Energy in the Sub-Mesoscale Range on the Black Sea Shelf and in Its Central Part. Physical Oceanography, 28(1). https://doi.org/10.22449/1573-160X-2021-1-37-51

Qiu, B., Chen, S., Klein, P., Wang, J., Torres, H., Fu, L.-L., & Menemenlis, D. (2018). Seasonality in Transition Scale from Balanced to Unbalanced Motions in the World Ocean. *Journal of Physical Oceanography*, *48*(3), 591–605. https://doi.org/10.1175/JPO-D-17-0169.1

Qiu, B., Nakano, T., Chen, S., & Klein, P. (2022). Bi-Directional Energy Cascades in the Pacific Ocean From Equator to Subarctic Gyre. *Geophysical Research Letters*, *49*(8). https://doi.org/10.1029/2022GL097713

Rocha, C. B., Gille, S. T., Chereskin, T. K., & Menemenlis, D. (2016). Seasonality of submesoscale dynamics in the Kuroshio Extension. *Geophysical Research Letters*, *43*(21).

https://doi.org/10.1002/2016GL071349

Schubert, R., Gula, J., Greatbatch, R. J., Baschek, B., & Biastoch, A. (2020). The Submesoscale Kinetic Energy Cascade: Mesoscale Absorption of Submesoscale Mixed Layer Eddies and Frontal Downscale Fluxes. *Journal of Physical Oceanography*, *50*(9), 2573–2589. https://doi.org/10.1175/JPO-D-19-0311.1

Shaw, P.-T. (1989). The intrusion of water masses into the sea southwest of Taiwan. *Journal of Geophysical Research*, *94*(C12), 18213. https://doi.org/10.1029/JC094iC12p18213

Sheremet, V. A. (2001). Hysteresis of a Western Boundary Current Leaping across a Gap. *Journal of Physical Oceanography*, *31*(5), 1247–1259. https://doi.org/10.1175/1520-0485(2001)031<1247:HOAWBC>2.0.CO;2

Srinivasan, K., Barkan, R., & McWilliams, J. C. (2022). *A forward energy flux at submesoscales driven by frontogenesis* (preprint). Oceanography. https://doi.org/10.1002/essoar.10509991.1

Su, J. (2004). Overview of the South China Sea circulation and its influence on the coastal physical oceanography outside the Pearl River Estuary. *Continental Shelf Research*, *24*(16), 1745–1760. https://doi.org/10.1016/j.csr.2004.06.005

Su, Z., Wang, J., Klein, P., Thompson, A. F., & Menemenlis, D. (2018). Ocean submesoscales as a key component of the global heat budget. *Nature Communications*, *9*(1), 775. https://doi.org/10.1038/s41467-018-02983-w

Sun, Z., Zhang, Z., Qiu, B., Zhang, X., Zhou, C., Huang, X., et al. (2020). Three-Dimensional Structure and Interannual Variability of the Kuroshio Loop Current in the Northeastern South China Sea. *Journal of Physical Oceanography*, *50*(9), 2437–2455. https://doi.org/10.1175/JPO-D-20-0058.1

Thomas, L. N., Tandon, A., & Mahadevan, A. (2008). Submesoscale processes and dynamics. In M. W. Hecht & H. Hasumi (Eds.), *Geophysical Monograph Series* (Vol. 177, pp. 17–38). Washington, D. C.: American Geophysical Union. https://doi.org/10.1029/177GM04

Thompson, A. F., Lazar, A., Buckingham, C., Naveira Garabato, A. C., Damerell, G. M., & Heywood, K. J. (2016). Open-Ocean Submesoscale Motions: A Full Seasonal Cycle of Mixed Layer Instabilities from Gliders. *Journal of Physical Oceanography*, *46*(4), 1285–1307. https://doi.org/10.1175/JPO-D-15-0170.1

Tian, J., Yang, Q., & Zhao, W. (2009). Enhanced Diapycnal Mixing in the South China Sea. *Journal of Physical Oceanography*, *39*(12), 3191–3203. https://doi.org/10.1175/2009JPO3899.1

Wang, G. (2003). Mesoscale eddies in the South China Sea observed with altimeter data. *Geophysical Research Letters*, *30*(21), 2121. https://doi.org/10.1029/2003GL018532

Yang, Q., Zhao, W., Liang, X., & Tian, J. (2016). Three-Dimensional Distribution of Turbulent Mixing in the South China Sea. *Journal of Physical Oceanography*, *46*(3), 769–788. https://doi.org/10.1175/JPO-D-14-0220.1

Yu, X., Naveira Garabato, A. C., Martin, A. P., Buckingham, C. E., Brannigan, L., & Su, Z. (2019). An Annual Cycle of Submesoscale Vertical Flow and Restratification in the Upper Ocean. *Journal of Physical Oceanography*, *49*(6), 1439–1461. https://doi.org/10.1175/JPO-D-18-0253.1

Zhang, J., Zhang, Z., Qiu, B., Zhang, X., Sasaki, H., Zhao, W., & Tian, J. (2021). Seasonal Modulation of Submesoscale Kinetic Energy in the Upper Ocean of the Northeastern South China Sea. *Journal of Geophysical Research: Oceans*, *126*(11).

https://doi.org/10.1029/2021JC017695

Zhang, X., Zhang, Z., McWilliams, J. C., Sun, Z., Zhao, W., & Tian, J. (2022). Submesoscale Coherent Vortices Observed in the Northeastern South China Sea. *Journal of Geophysical Research: Oceans*, *127*(2), e2021JC018117. https://doi.org/10.1029/2021JC018117

Zhang, Z., Tian, J., Qiu, B., Zhao, W., Chang, P., Wu, D., & Wan, X. (2016). Observed 3D Structure, Generation, and Dissipation of Oceanic Mesoscale Eddies in the South China Sea. *Scientific Reports*, *6*(1), 24349. https://doi.org/10.1038/srep24349

Zhang, Z., Zhao, W., Qiu, B., & Tian, J. (2017). Anticyclonic Eddy Sheddings from Kuroshio Loop and the Accompanying Cyclonic Eddy in the Northeastern South China Sea. *Journal of Physical Oceanography*, *47*(6), 1243–1259. https://doi.org/10.1175/JPO-D-16-0185.1

Zhang, Z., Zhang, Y., Qiu, B., Sasaki, H., Sun, Z., Zhang, X., et al. (2020). Spatiotemporal Characteristics and Generation Mechanisms of Submesoscale Currents in the Northeastern South China Sea Revealed by Numerical Simulations. *Journal of Geophysical Research: Oceans*, *125*(2), e2019JC015404. https://doi.org/10.1029/2019JC015404

Zhang, Z., Zhang, X., Qiu, B., Zhao, W., Zhou, C., Huang, X., & Tian, J. (2021). Submesoscale Currents in the Subtropical Upper Ocean Observed by Long-Term High-Resolution Mooring Arrays. *Journal of Physical Oceanography*, *51*(1), 187–206. https://doi.org/10.1175/JPO-D-20-0100.1

Zhang, Z., Liu, Y., Qiu, B., Luo, Y., Cai, W., Yuan, Q., et al. (2023). Submesoscale inverse energy cascade enhances Southern Ocean eddy heat transport. *Nature Communications*, *14*(1), 1335. https://doi.org/10.1038/s41467-023-36991-2

Zhong, Y., Bracco, A., Tian, J., Dong, J., Zhao, W., & Zhang, Z. (2017). Observed and simulated submesoscale vertical pump of an anticyclonic eddy in the South China Sea. *Scientific Reports*, *7*(1), 44011. https://doi.org/10.1038/srep44011

Figures

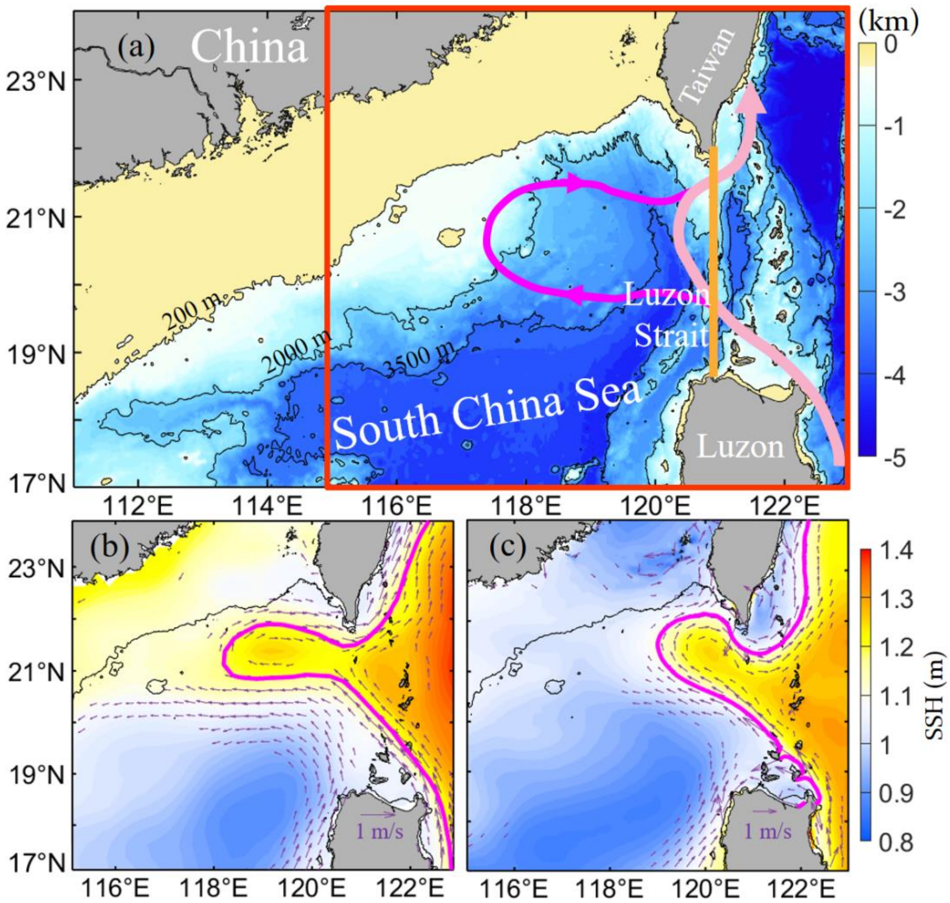

Figure 1. (a) Bathmetry in the northern South China Sea. Purple and pink lines represent the looping and leaping paths of Kuroshio, respectively. The isobaths of 200, 2000, and 3500 m are denoted using black lines. Red box marks the study region, i.e., NESCS. Solid orange line represents the 120.8 °E section. (b) Distribution of altimeter observed sea surface height (SSH) averaged in the winters (December, January, and February) of 1999–2000, 2011–2012, 2016–2017, 2017–2018 when prominent KLC occurred. Purple arrows are the corresponding absolute geostrophic velocity at surface with magnitude larger than 0.2 m/s. (c) Same as (b) but for the result from the LLC4320 simulation. Purple lines in (b, c) are the SSH contours of

1.19 m and 1.12 m, respectively, which roughly depict the path of KLC.

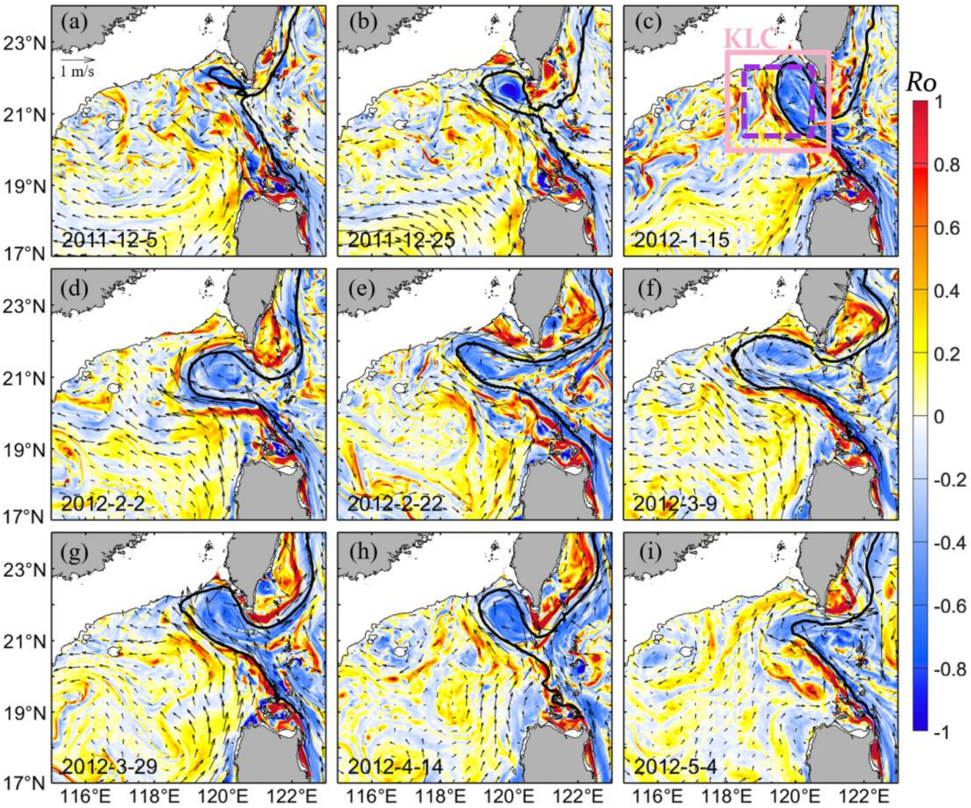

Figure 2. Distributions of the daily-averaged Rossby number (color shading) and current velocities (black arrows) at 5-m depth from the LLC4320 data. Regions with water depth shallower than 200 m are masked using blank. The date is marked on the left-bottom corner of each panel. Black thick line denotes the main axis of the KLC, which is defined as the SSH contour with highest mean salinity at 150 m. Pink solid box marks the KLC region. Purple dashed box marks a smaller KLC region where the main part of KLC exists.

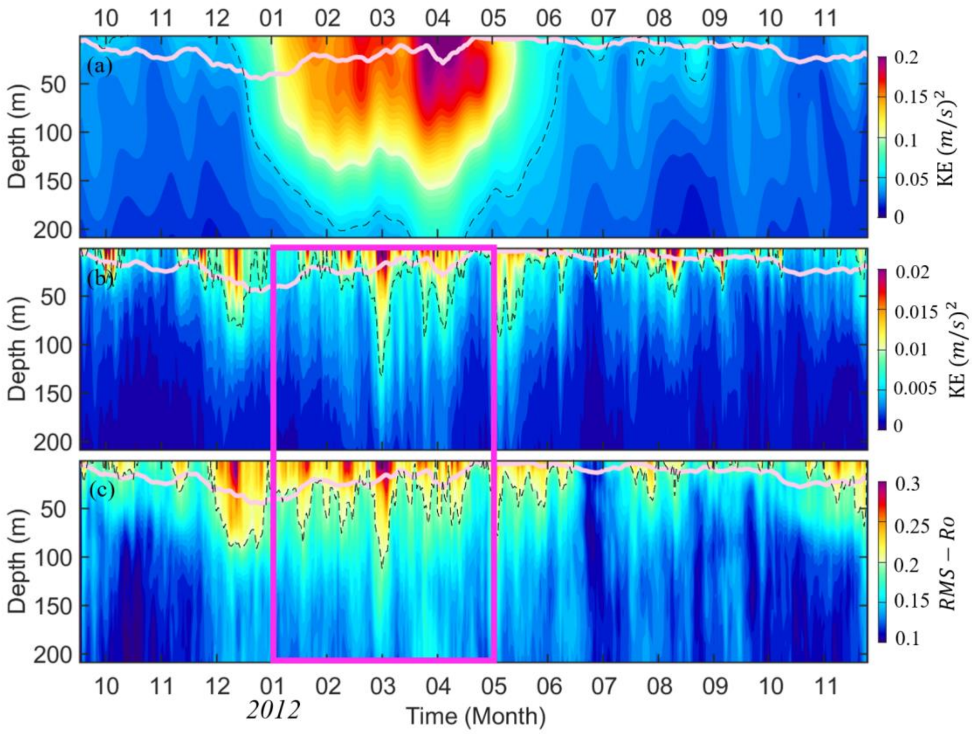

Figure 3. Depth-time plot of (a) meso- to large- scale (i.e., larger-scale) KE, (b) submesoscale KE, and (c) root-mean-squared submesoscale *Ro*. The results are averaged over the KLC region denoted by the pink solid box in Figure 2c. Pink solid line denotes the base of mixed layer averaged in the KLC region. Black dashed lines in (a, b, c) are contours of 0.05 m^2/s^2, 0.008 m^2/s^2, and 0.2, respectively. Purple square in (b, c) denotes the main period of the KLC.

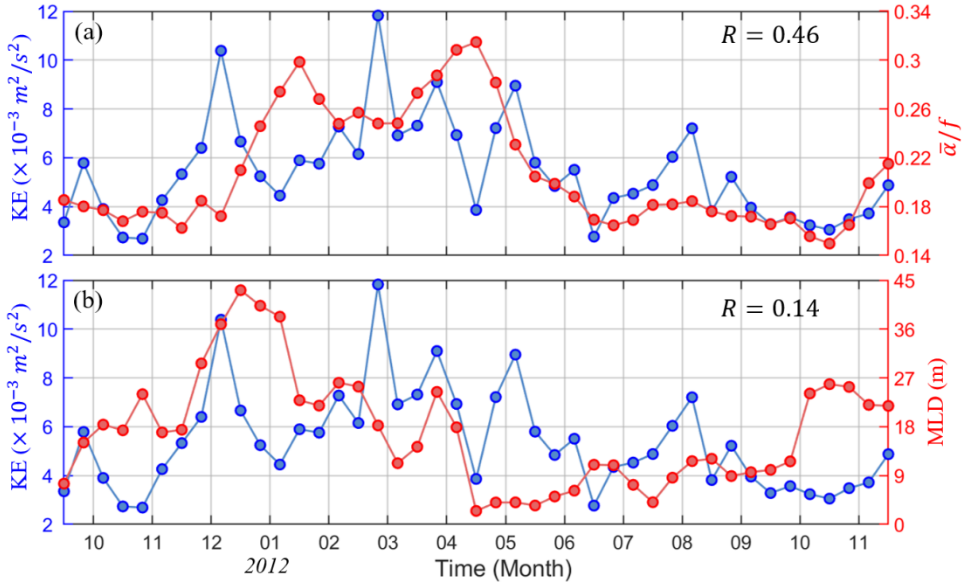

Figure 4. (a) Comparison between upper 100-m-averaged submesoscale KE (blue; y-axis on the left) and larger-scale strain rate normalized by dividing f (red; y-axis on the right) averaged in the KLC region denoted by the pink solid box in Figure 2c. Both the time series are weekly average and their correlation coefficient is marked on the right-top corner (R = 0.094 for the 95% confidence level). (b) Same as (a) except that the red line denotes the MLD.

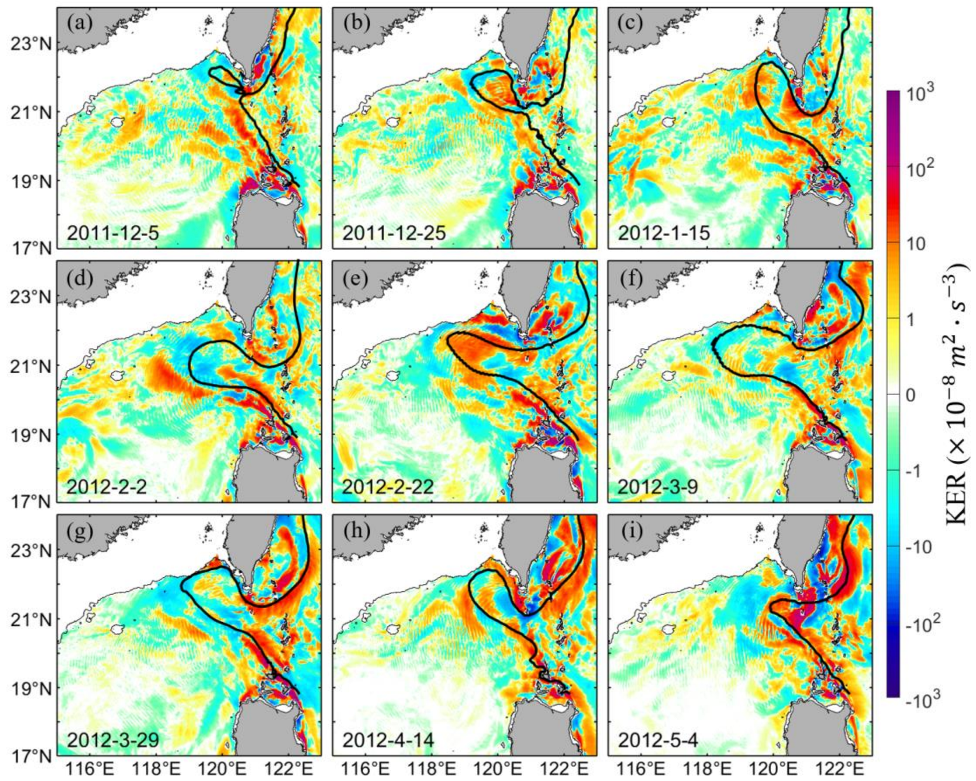

Figure 5. Same as Figure 2 but for the upper 100-m and 15-day averaged KER. Note that values in the color bar is logarithmic.

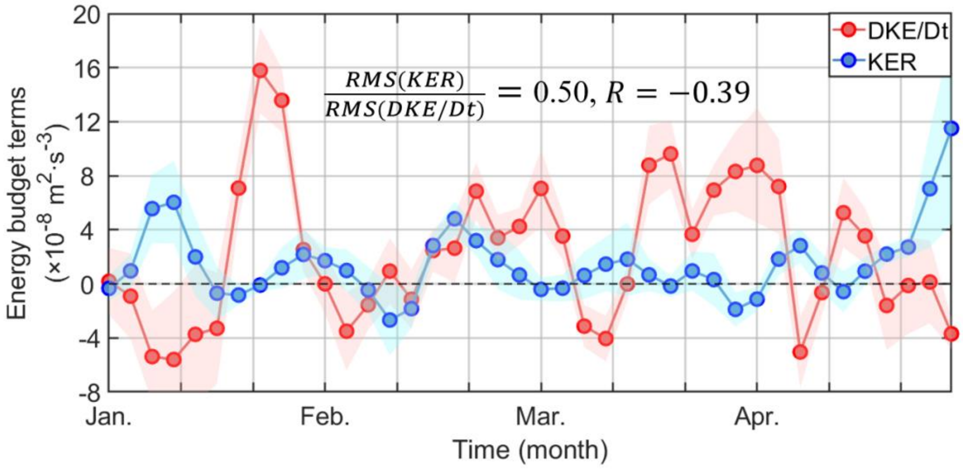

Figure 6. Comparison between the upper 100-m-averaged KER (blue) and material derivative of larger-scale KE (red; i.e., DKE/Dt) averaged in the KLC region. The dots are 3-day averages. Ratio between the RMS values of KER and DKE/Dt and correlation coefficient between their time series are marked (R = -0.18 for the 95% confidence level). The shadings denote the 95% confidence intervals of the corresponding solid lines calculated using bootstrap method.

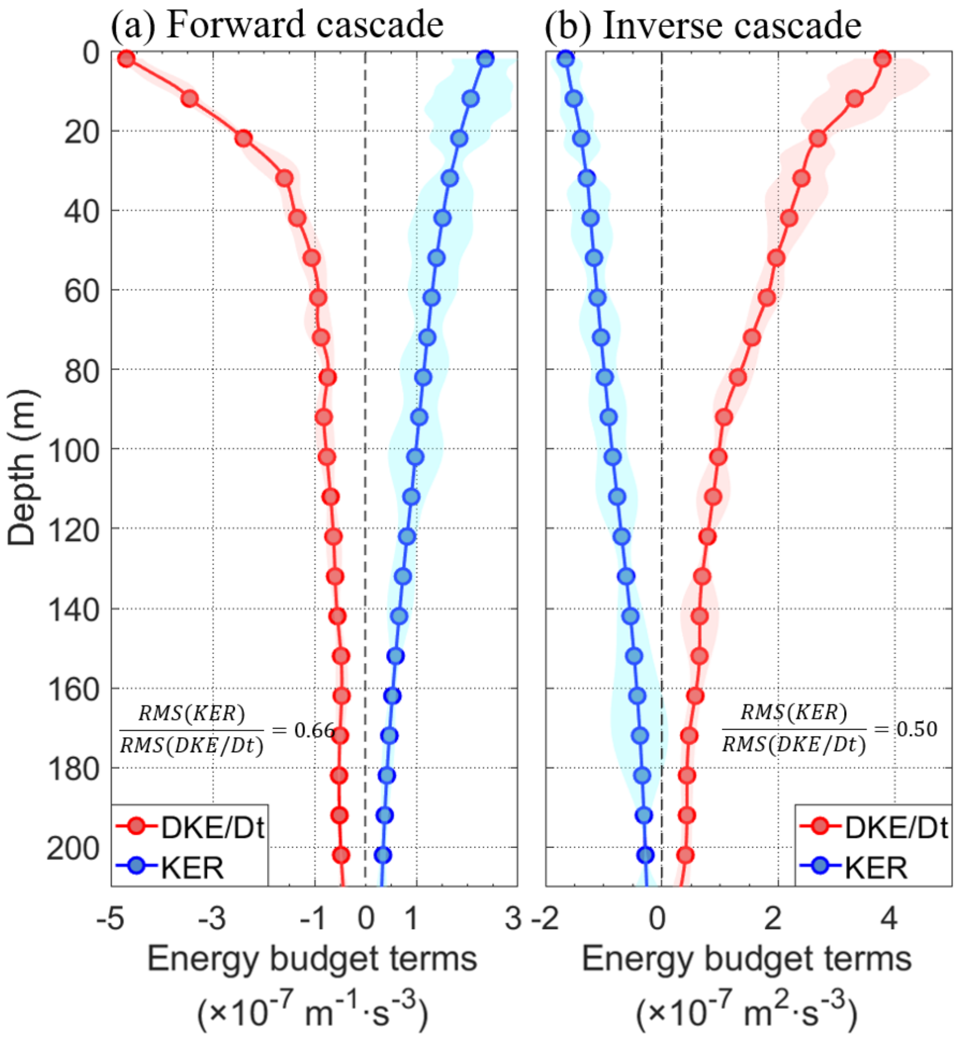

Figure 7. (a) Compositely mean vertical profiles of KER (blue) and DKE/Dt (red) when forward cascade occurs (i.e., KER>0) during the KLC period. The results are averaged in the KLC region. (b) Same as (a) but for the situation of inverse cascade (i.e., KER<0) The shadings denote the 95% confidence intervals of the corresponding solid lines calculated using bootstrap method. Ratio between the RMS values of KER and DKE/Dt is marked.

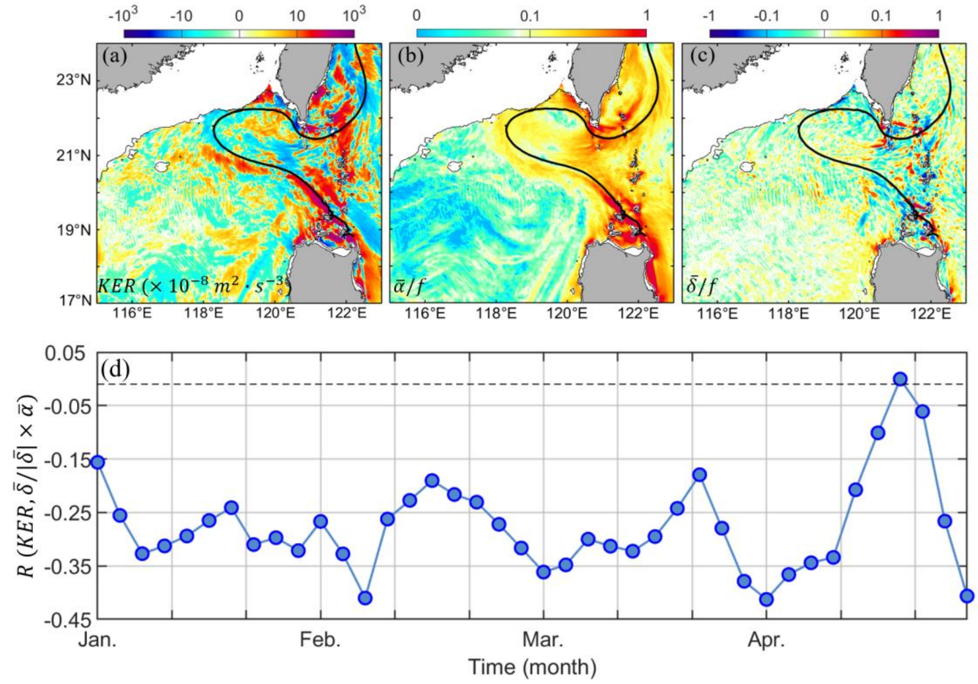

Figure 8. Distributions of (a) KER, (b) $\bar{\alpha}/f$, and (c) $\bar{\delta}/f$ at 5-m depth averaged in March, 2012. Regions with water depth shallower than 200 m are masked using blank. Black thick line denotes the main axis of KLC (same meaning with those in Figure 2). Color bars are all expressed in logarithmic scale. (d) Time-dependent correlation coefficients between KER and $\bar{\delta}/|\bar{\delta}|\times\bar{\alpha}$ at 5-m depth calculated using all grid points in the KLC region at each time step (i.e., 3-day average). Black dashed line represents the 95% confidence level.

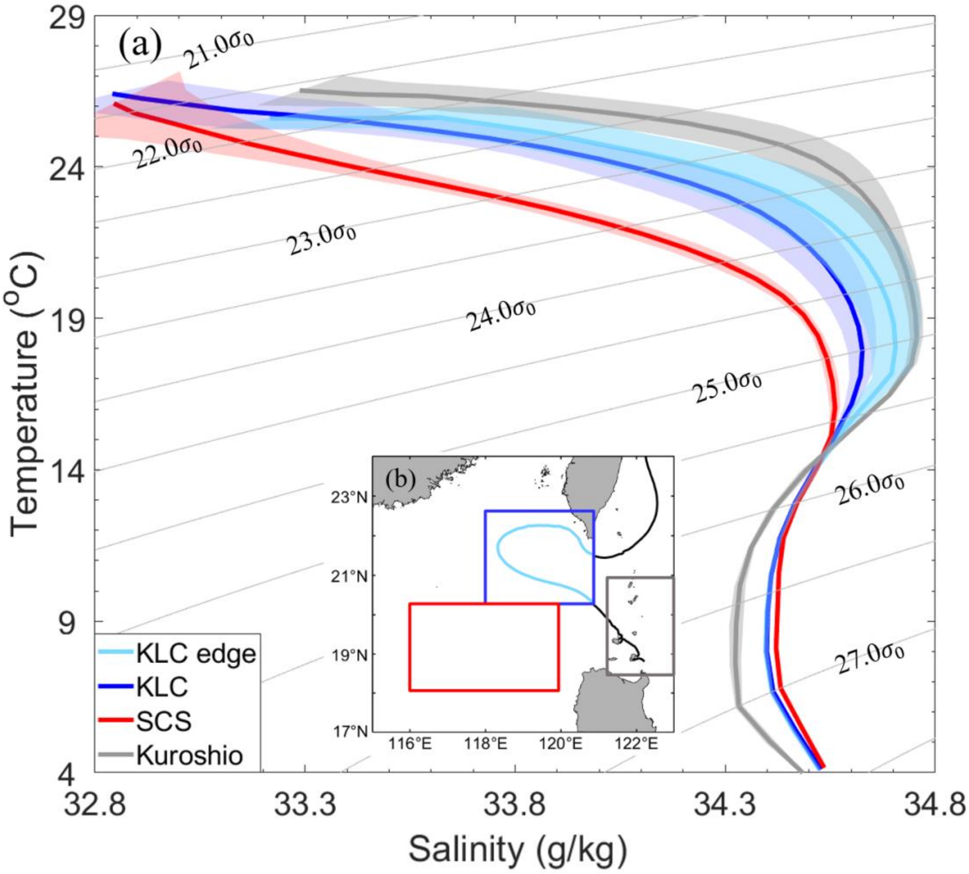

Figure 9. *T-S* diagrams of different water masses in the NESCS and Luzon Strait derived from the LLC4320 data. Solid lines and color shadings denote the mean *T-S* curves and their standard deviations during the KLC period, respectively. Red, gray, dark blue, and light blue lines denote the NESCS water, the Kuroshio water, and waters in the KLC region and at the KLC edge, respectively. The spatial scopes of different water masses are marked using squares or curve in (b) with same colors with the corresponding *T-S* curves in (a). The gray oblique lines in (a) are isopycnic lines from 21.0 σ_0 to 27.5 σ_0.

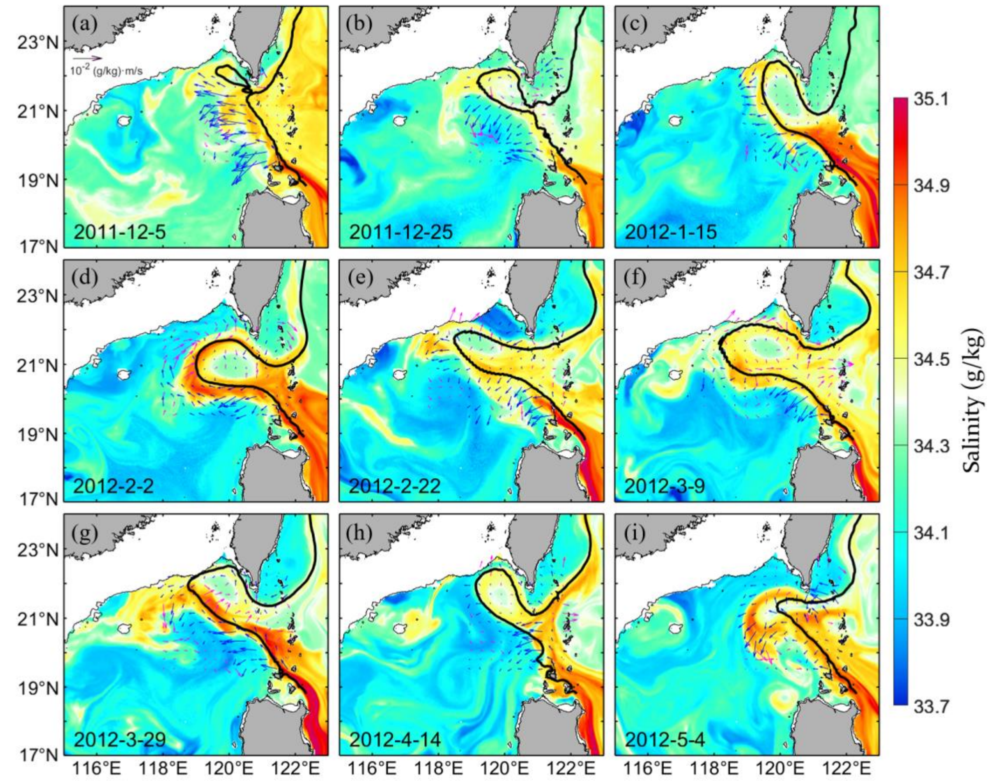

Figure 10. Same as Figure 5 but for the 15-day-averaged salinity (color shading) and divergence component of submesoscale salt flux ($\boldsymbol{SF_D}$; arrows) on the $23.5\,\sigma_0$ isopycnal. Blue and purple arrows denote that $\boldsymbol{SF_D}$ has a westward and eastward zonal component, respectively.

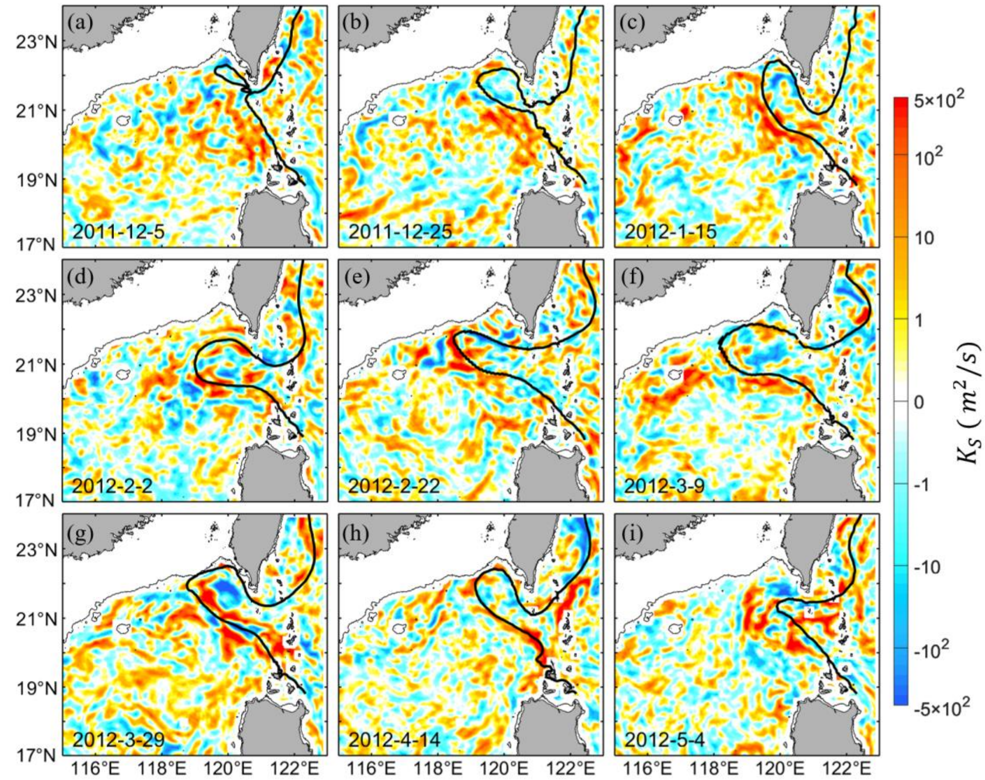

Figure 11. Same as Figure 10 but for the submesoscale salt diffusivity (i.e., K_S) on the $23.5\sigma_0$ isopycnal. Note that color bar is expressed in logarithmic scale.

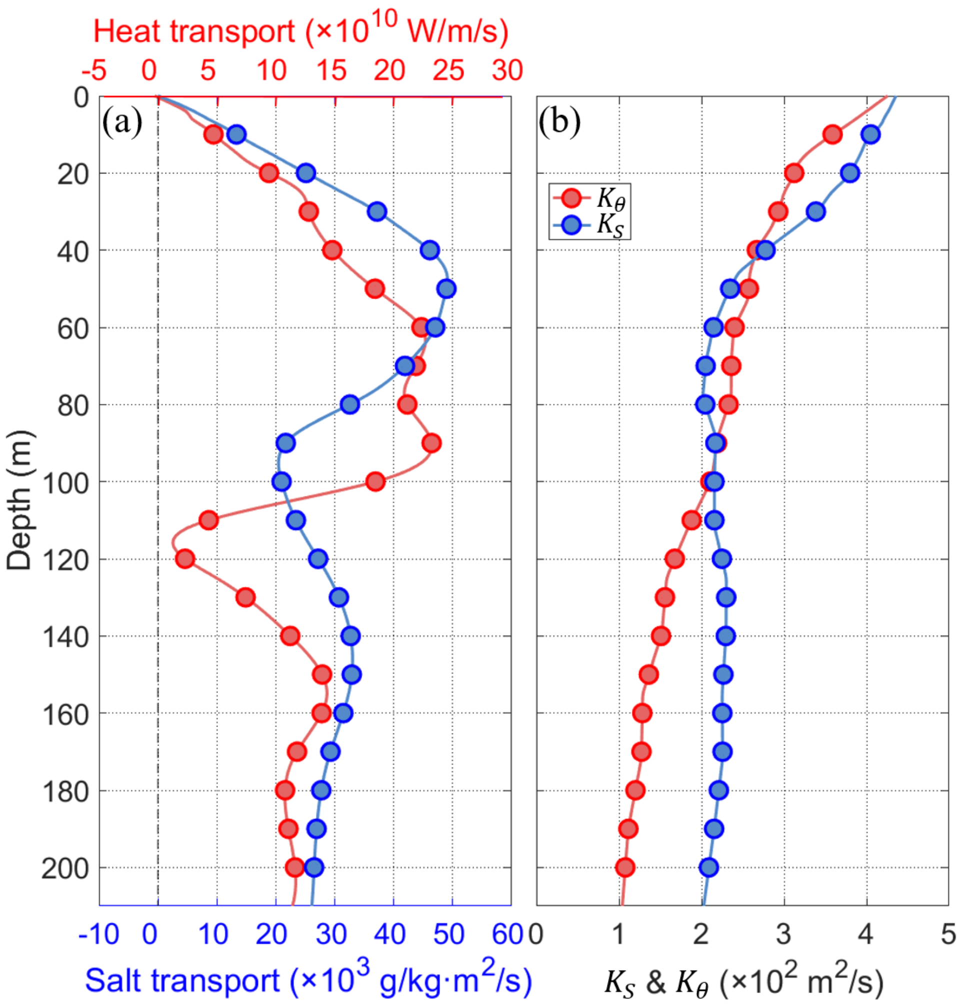

Figure 12. (a) Vertical profiles of submesoscales-induced salt and heat transports per unit depth (i.e., STD and HTD) westward across the KLC main axis west of 120.8 °E. The results are averaged in March, 2012 when the KLC is at its mature stage. (b) Same as (a) but for the K_S (blue) and K_θ (red) averaged along the KLC main axis.

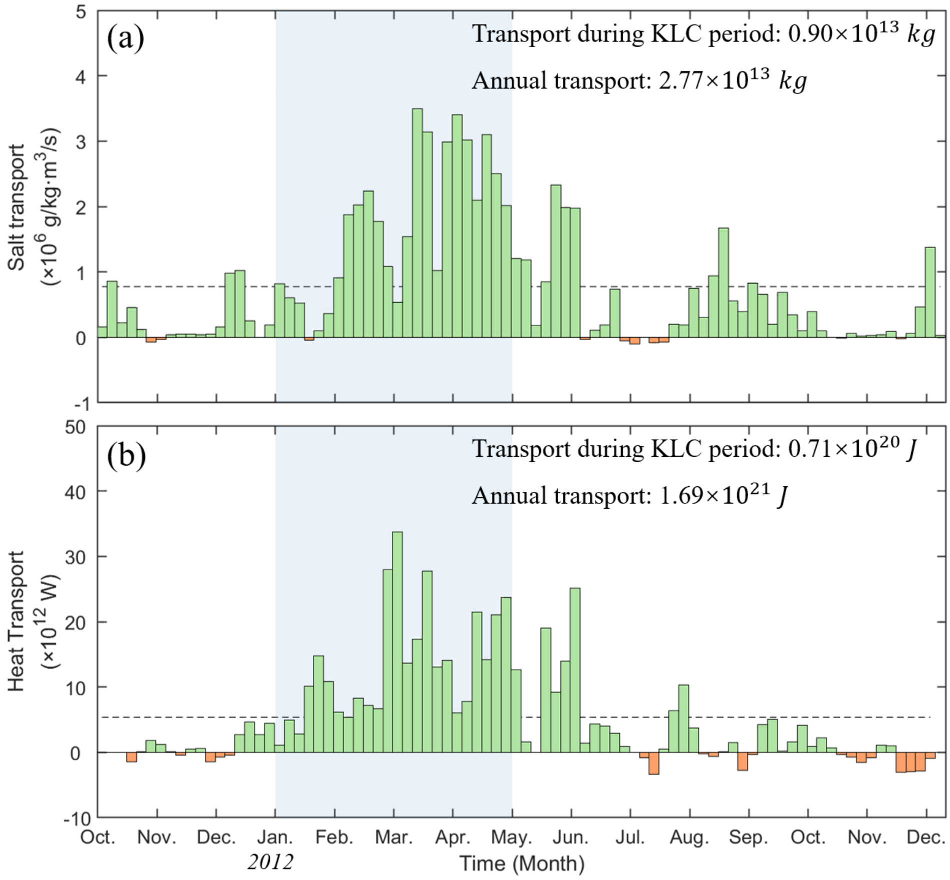

Figure 13. (a) Five-day averaged and vertically integrated submesoscale salt transport (i.e., IST) westward across the Kuroshio main axis (i.e., the SSH contour with the highest average salinity at 150 m) near the Luzon Strait. Positive and negative values denote westward and eastward directions, respectively. Blue shading marks the KLC period. The salt transports during the KLC period and throughout the year (between October 1th, 2011 and September 30th, 2012) are marked in the upper right corner. (b) Same as (a) but for the vertically integrated submesoscale heat transport (i.e., IHT). Black dashed lines in (a, b) indicate the mean values throughout the 14-month data period (i.e., $7.80{\times}10^5$ g/kg·m^3/s and $5.36{\times}10^{12}$ W).